RSC Advances

PAPER

View Article Online
View Journal | View Issue

Cite this: *RSC Adv.*, 2017, 7, 45997

Biodistribution of upconversion/magnetic silica-coated NaGdF$_4$:Yb^{3+}/Er^{3+} nanoparticles in mouse models†

Uliana Kostiv,[a] Lenka Rajsiglová,[b] Dominika Luptáková,[b] Tomáš Pluháček,[b] Luca Vannucci,*[b] Vladimír Havlíček,[b] Hana Engstová,[b] Daniel Jirák,[cd] Miroslav Šlouf,[a] Peter Makovicky,[e] Radislav Sedláček[e] and Daniel Horák*[a]

Nanoparticles are constructs that can be used for cellular interventions and targeted drug delivery. They are useful for overcoming the dose-related toxic effects of drugs or diagnostic preparations by predominant or selective accumulation in the pathologic tissues. Gadolinium(III) compounds are largely used as contrast agents in magnetic resonance imaging (MRI) but may have toxic effects, especially in nephropathic patients, due to the dose required for use in MRI. Here, we describe the preparation of new multifunctional NaGdF$_4$:Yb^{3+}/Er^{3+} nanoparticles, their characteristic properties, and some preliminary data about their effect on cell viability and tissue localization. Hexagonal-phase NaGdF$_4$ nanocrystals that were doped with optically active Yb^{3+} and Er^{3+} ions, were synthesized by coprecipitation of lanthanide chlorides in octadec-1-ene at high temperature, stabilized by oleic acid, and subsequently coated with a thin silica layer. The morphology, elemental composition, crystalline structure, and SiO$_2$ coating of the prepared NaGdF$_4$:Yb^{3+}/Er^{3+}@SiO$_2$ nanoparticles were characterized in detail by transmission electron microscopy (TEM) combined with energy-dispersive spectroscopy (TEM/EDX) and selected area electron diffraction (TEM/SAED) and attenuated total reflection Fourier transform infrared (ATR FTIR) spectroscopy. The upconversion and paramagnetic properties of the particles were measured using confocal microscopy and MRI, respectively. The biocompatibility of the NaGdF$_4$:Yb^{3+}/Er^{3+}@SiO$_2$ nanoparticles was tested *in vitro* using mouse 3T3 fibroblasts and B16F10 melanoma cells. Particle localization was evaluated *ex vivo* in tumor, liver, and brain tissues of B16F10 melanoma bearing mice after intravenous administration. The NaGdF$_4$:Yb^{3+}/Er^{3+}@SiO$_2$ particles proved to be non-toxic at moderate concentrations. Particle localization within the organs was demonstrated by analysis of the tissues using laser ablation inductively coupled plasma mass spectrometry (LA-ICP-MS) and showed vascular localization.

Received 7th August 2017
Accepted 19th September 2017

DOI: 10.1039/c7ra08712h

rsc.li/rsc-advances

1. Introduction

Lanthanide-based nanocrystals have gained considerable attention for various biological applications due to their unique luminescent and magnetic properties, which can be easily controlled by varying the lanthanide ion dopants.[1–3] In particular, upconversion/magnetic NaGdF$_4$:Yb^{3+}/Er^{3+} nanoparticles have great potential as promising multimodal probes for *in vitro* and *in vivo* bioimaging,[4] targeted drug delivery,[5] and image-guided surgery.[6] Due to the presence of optically active Yb^{3+}/Er^{3+} ion pair in the Gd^{3+}-containing host lattice, the particles show not only a strong near-infrared (NIR) to visible upconversion luminescence but also a short longitudinal relaxation time T_1 that allows simultaneous optical and magnetic resonance (MR) images of healthy and diseased tissues.[6–8] Moreover, the maximum light absorption of the NaGdF$_4$:Yb^{3+}/Er^{3+} nanoparticles falls within the "optical window" of the biological tissues. The advantages of the particles include a large anti-Stokes shift of ~500 nm, absence of photobleaching and photoblinking, weak autofluorescence, deep light penetration, and reduced photodamage to living organisms.[9,10] Integration of the magnetic and upconversion features in one particle provides more detailed and accurate non-invasive imaging information

---

[a] Institute of Macromolecular Chemistry, Academy of Sciences of the Czech Republic, Heyrovského nám. 2, 162 06 Prague 6, Czech Republic

[b] Institute of Microbiology, Academy of Sciences of the Czech Republic, Vídeňská 1083, 142 20 Prague 4, Czech Republic

[c] Radiodiagnostic and Interventional Radiology Department, Institute for Clinical and Experimental Medicine, Vídeňská 1958/9, 140 21 Prague, Czech Republic

[d] Department of Biophysics, Institute of Biophysics and Informatics, First Faculty of Medicine, Charles University, Salmovská 1, 120 00 Prague 2, Czech Republic

[e] Czech Centre for Phenogenomics, Institute of Molecular Genetics, Academy of Sciences of the Czech Republic, 252 50 Vestec, Czech Republic

† Electronic supplementary information (ESI) available: T_1 relaxometry (Table S1), calibration curves (Fig. S1), and size distribution histograms (Fig. S2). See DOI: 10.1039/c7ra08712h

than using each method alone, facilitating diagnoses and follow-up therapeutic responses over long time periods.

Biocompatibility, dispersibility in water, and uniform particle size are prerequisite conditions to meet the demands of biomedical applications. Currently, $NaGdF_4:Yb^{3+}/Er^{3+}$ nanoparticles are generally synthetized by high-temperature coprecipitation of lanthanide chlorides in an organic solvent, *e.g.*, octadec-1-ene, and stabilized by oleic acid.[11] However, these particles are hydrophobic and lack functional groups, which presents an obstacle for further surface conjugation of targeting ligands and therapeutic agents. Surface chemistry thus remains a key issue to minimize nonspecific uptake by the reticuloendothelial system, prolong blood circulation time, and improve diagnostic efficiency. Strategies to design water-dispersible particles include ligand exchange[12] or oxidation,[13] and encapsulation with SiO_2 or polymers.[14,15]

Gd is a paramagnetic lanthanide that was used more than 30 years ago in the formulation of contrast agents to enhance contrast in magnetic resonance imaging (MRI) due to its large magnetic moment and short relaxation time.[16] Once in the circulation after intravenous administration, it demarks the vascularization of an organ and is widely used for magnetic resonance angiography. However, compromised kidney function is a contra-indication to its administration because Gd filtration is inefficient. Subsequent systemic toxicity is possible, even leading to fatal nephrogenic systemic fibrosis.[17]

Studies during the last twenty years have demonstrated the importance of the tumor microenvironment and of therapeutic interventions specifically directed toward cancer cells, infiltrating and surrounding immune cells, stroma cells, stromal structures, vessels, nerves and soluble products.[18] A targeted therapy is not only critical to achieve highly efficient anticancer effects but also necessary to reduce unwanted side reactions in the rest of the organism. At present, the development of nanotherapeutics allows a selective targeting of the cancer cells and the tumor microenvironment. The availability of diagnostic tracers, *e.g.*, gold, iron oxide, gadolinium,[19,20] or human ferritin loaded with maghemite[21,22] as carriers of therapeutic agents has opened the field of theranostics, in which the dual functions of diagnosis and therapy are combined in a single nanoconstruct.[23] Moreover, a selective targeting of tumors can be obtained through the enhanced permeability and retention effect (EPR) due to endothelial leakages in the tumor neovascularization[24] and the reduced lymphatic circulation in the tumor microenvironment with possibility to reach concentrations 5–10 times higher than in normal tissue within 1–2 days.[25] Imaging of tumor vascularization and identification of the sites of EPR can help in deciding the type of tumor targeting, as well as the opportunity for anti-angiogenic therapy.

In our study, we synthesized $NaGdF_4:Yb^{3+}/Er^{3+}@SiO_2$ nanoparticles and evaluated them in the context of achieving a new system that, while reducing the general toxic effects by lowering the diagnostic dose, may maintain an efficient vascular localization. This might lead to targeted treatment of cancer or even other pathologies with aggressive neo-vascularization, such as neo-vascular eye diseases.[26] For a preliminary evaluation, three main tissues were analyzed (tumor, liver, and brain) as examples of different vascular conditions: neo-angiogenesis, regular and abundant vascularization associated with reticular-endothelial cells, and vascularization with restricted permeability due to the brain–blood barrier. Biocompatibility, *i.e.*, cell viability, was also tested *in vitro* on tumor and non-tumor mouse cell lines and on immune cells.

2. Experimental

2.1 Chemicals

Lanthanide chlorides, such as anhydrous gadolinium(III), ytterbium(III), and erbium(III) chloride (99%), octadec-1-ene (90%), ammonium fluoride, tetramethoxysilane (TMOS), and Igepal CO-520 [polyoxyethylene (5) nonylphenylether], were purchased from Sigma-Aldrich (St. Louis, MO, USA). Sodium hydroxide was acquired from Lach-Ner (Neratovice, Czech Republic), and oleic acid, methanol, ethanol, and acetone were acquired from Lachema (Brno, Czech Republic). The 3-(4,5-dimethylthiazol-2-yl)-2,5-diphenyltetrazolium bromide (MTT) assay was purchased from Serva Electrophoresis GmbH (Heidelberg, Germany). Ultrapure Q-water (pH 7; resistivity 18.2 MΩ cm) produced using ultrafiltration on a Milli-Q Gradient A10 system (Millipore; Molsheim, France) was used in all experiments.

2.2 Synthesis of $NaGdF_4:Yb^{3+}/Er^{3+}$ nanoparticles

$NaGdF_4:Yb^{3+}/Er^{3+}$ nanoparticles were prepared according to previously described procedure with some modifications.[27,28] In a typical synthesis, 1 mmol of lanthanide chloride (0.78 mmol $GdCl_3$, 0.2 mmol $YbCl_3$, and 0.02 mmol $ErCl_3$) was placed in a 100 ml three-neck flask to which octadec-1-ene (15 ml) and oleic acid stabilizer (6 ml) were added. The flask was heated to 160 °C for 30 min to obtain a homogenous solution and cooled to room temperature (RT), after which a methanolic solution (5 ml) containing NH_4F (4 mmol) and NaOH (4 mmol) was added dropwise. The resulting mixture was slowly heated to 70 °C until all the methanol evaporated, stirred under a gentle flow of argon, and heated to 300 °C for 90 min. After cooling to RT, the resulting $NaGdF_4:Yb^{3+}/Er^{3+}$ nanoparticles were precipitated in acetone (30 ml), separated using a Sorvall Legend X1 centrifuge (ThermoFisher; Osterode, Germany), washed three times with ethanol, separated by centrifugation, and stored in hexane.

2.3 Synthesis of $NaGdF_4:Yb^{3+}/Er^{3+}@SiO_2$ nanoparticles

The surfaces of the $NaGdF_4:Yb^{3+}/Er^{3+}$ nanoparticles were coated with silica using a microemulsion technique.[29] $NaGdF_4:Yb^{3+}/Er^{3+}$ nanoparticles (30 mg) were dispersed in hexane (10 ml) and Igepal CO-520 (0.5 ml) and 25% aqueous ammonia (80 µl) were added. After sonication for 20 min, a stable emulsion was formed; TMOS (20 µl) was added and the mixture was stirred (600 rpm) at RT for 2 days. The resulting $NaGdF_4:Yb^{3+}/Er^{3+}@SiO_2$ particles were precipitated with acetone (5 ml), washed three times with water/ethanol (1 : 1 v/v), and stored in water.

2.4 Viability test of cells incubated with $NaGdF_4:Yb^{3+}/Er^{3+}@SiO_2$ nanoparticles

Murine B16F10 melanoma and fetal 3T3 fibroblast cell lines (ATCC; Manassas, VA, USA) were used to evaluate the possible cytotoxic effects and biocompatibility of $NaGdF_4:Yb^{3+}/Er^{3+}@SiO_2$ nanoparticles using the MTT cell viability assay. The 3T3 cells were used not only as a common model of non-tumor cells, but also because fibroblasts are important component of the tumor microenvironment.[30] The cells were cultured at 37 °C under a 5% CO_2 atmosphere in Dulbecco's modified Eagle medium (DMEM; Institute of Molecular Genetics; Prague, Czech Republic) supplemented with 2 mM L-glutamine, 0.05 mg gentamycin, 1 mM sodium pyruvate, 0.05 mM 2-mercaptoethanol (Sigma-Aldrich) and 10% heat-inactivated fetal calf serum (FCS; Gibco; Grand Island, NY, USA).

Male Balb/c mice (Institute of Physiology, Prague, Czech Republic) were used. After adaptation to the conditions of local animal facility (Institute of Microbiology, Prague, Czech Republic), the spleen from a Balb/c mouse was harvested in sterile conditions into HMEM-d culture medium (Institute of Molecular Genetics). After mashing through a nylon net, half of the splenocytes was separated on the Ficoll-PaqueTM 1085 (GE HealthCare; Stockholm, Sweden) using gradient density centrifugation (500 g/30 min at 18 °C) to isolate the mononuclear cells; the other half was used unseparated to include myeloid cells. Both types of splenocyte suspensions were then transferred to DMEM for culture.

The original colloid (2 mg of $NaGdF_4:Yb^{3+}/Er^{3+}@SiO_2$/ml) was diluted 50-fold in a phosphate-buffered solution (PBS) to avoid aggregation of the particles and sterilized using UV light. Further dilutions were obtained from this stock dispersion to evaluate the effect of the $NaGdF_4:Yb^{3+}/Er^{3+}@SiO_2$ particles at the different concentrations. Cells were seeded on 96-well plates in 150 μl of media at concentrations ranging from 20 000 to 30 000 cells per well. In the next step, the cells were incubated in the presence of 4.4, 22 or 44 ng of particles per well (equivalent to 0.03, 0.15 and 0.3 mg ml^{-1}), or 2.2, 22 or 45 μg of nanoparticles per well (corresponding to 0.015, 0.15 and 0.35 mg ml^{-1}). The cell viability was compared to control group in the absence of the nanoparticles. The tests were performed in triplicate, and 12 wells with medium alone were used as a blank. The cells were cultured in the incubator at 37 °C for 48 and/or 72 h under a 5% CO_2 atmosphere. The cell viability was evaluated by adding MTT (10 μl; 5 mg ml^{-1}) to each well containing the particles or control and to 6 wells containing only the medium. The plates were kept in the dark and incubated for 1 h longer. After formation of the formazan crystals, the color of which turned to violet, the medium (80 μl) was carefully removed using a multichannel pipette, and dimethylsulfoxide (130 μl) was added to each well to dissolve the formazan crystals. The optical densities were obtained using a plate-reading spectrophotometer at 530 nm. The mean value of the blank (medium and MTT) was subtracted from each sample; the means and standard deviations for each group were determined using a Student's *t*-test; statistically significant results at $p \geq 0.05$ are shown in the graphs.

2.5 Animal model and localization of $NaGdF_4:Yb^{3+}/Er^{3+}@SiO_2$ nanoparticles in mouse organs

B16F10 melanoma cells (1×10^6) were subcutaneously inoculated into the lower back of syngeneic C57BL/6 mice (AnLab; Prague, Czech Republic), and the tumours were allowed to develop until they reached 10 mm in diameter. All experiments were approved by the Animal Care and Use Committee at the Institute of Microbiology (ID 64/2015). The animals were sacrificed 24 h after 3 intravenous injections (one per day every 24 h) of $NaGdF_4:Yb^{3+}/Er^{3+}@SiO_2$ nanoparticles (2 mg ml^{-1} at 1 : 50 dilution in sterile PBS). The volume of each administered dose was 100 μl.

Both tumor (melanoma) and healthy tissues (liver and brain) were snap-frozen immediately after harvesting and preserved at −80 °C. The Gd localization and amount in the samples was determined by laser ablation inductively coupled plasma mass spectrometry (LA-ICP-MS). The deeply frozen tissues were allowed to warm up to −13 °C prior to the sectioning with a Leica cryomicrotome CM1950 (Leica Biosystems; Wetzlar, Germany). The tissues were cut to 30 μm-thick slices for the quantitative LA-ICP-MS study of Gd and Fe distributions in the tissues, which were conducted using an Analyte G2 laser ablation unit (Photon Machines; Bozeman, MT, USA) equipped with an ArF excimer nanosecond laser (193 nm) coupled to a 7700× ORS-ICP-MS spectrometer (Agilent Technologies; Tokyo, Japan). An octupole reaction system working in helium mode was used to eliminate spectral interferences observed mainly on ^{56}Fe. The raw data (csv files) were transformed to the elemental distribution images using ImageLab multisensor imaging software (v. 2.18, Epina; Pressbaum, Austria). The elemental quantitative data were achieved by the analysis of a set of dried droplet calibration standards with the increasing concentration of both elements: 0, 5, 50, 100, 250, 500, and 1000 μg g^{-1} for Fe and 0, 0.1, 1, 10, 100, 500, and 1000 μg g^{-1} for Gd, respectively. The linear relationships were established with the correlation coefficients >0.993 for all calibration curves (Fig. S1 in ESI†).

The resulting images showing the $NaGdF_4:Yb^{3+}/Er^{3+}@SiO_2$ particle localization and accumulation in the tissue were compared with classical histology after haematoxylin and eosin staining performed on sequential sections. The Gd accumulations were expressed as a colorimetric gradient scale corresponding to the μg of accumulated Gd/g.

The tissue samples used in this analysis were evaluated to demonstrate the vascular net distribution by immunohistochemistry detection of endothelia. The samples were fixed in 4% formalin solution, stored at RT for 24 h, placed in a Leica ASP6025 automated tissue processor (Wetzlar, Germany), and embedded in paraffin blocks using a Leica EG 1150H paraffin embedding station. Slices (2–3 μm thick) were cut from each sample using a Leica RM2255 microtome and mounted on special glass slides. The first slices were stained with haematoxylin-eosin (DiaPath; Martinengo, Italy). The second set, for detection of the endothelial cells by immunohistochemistry methods, was performed using the anti-mouse CD31 (PECAM-1) antibody (Zytomed Systems; Berlin, Germany). 3,3′-Diaminobenzidine chromogen (Dako/Agilent; Glostrup, Denmark) was used for visualization of the detected vessels. The prepared slides were evaluated as light-microscopic images using a Carl Zeiss Axio Scope A1 (Oberkochen, Germany) and a Zeiss Axio Scan.Z1 slide scanner.

2.6 Characterization of the nanoparticles

Electron microscopy. The size, composition and crystal structure of the nanoparticles were analyzed using a Tecnai Spirit G^2 transmission electron microscope (TEM; FEI; Brno, Czech Republic). The microscope was equipped with an energy dispersive spectrometer (EDX; Mahwah, NJ, USA), which was used for the elemental analysis of the nanoparticles. Selected area electron diffraction (SAED) on the TEM microscope was used to verify the crystal structure of the nanoparticles. The electron diffraction patterns were processed using ProcessDiffraction software[31] and compared with the diffraction patterns calculated using PowderCell software;[32] the crystal structures for the diffraction pattern calculation were obtained from ICSD database.[33] Bright-field TEM micrographs were analyzed using Atlas software (Tescan; Brno, Czech Republic) to characterize the particle size distributions. Morphology of individual particles, including number-average diameter (D_n), weight-average diameter (D_w), uniformity (polydispersity index PDI = D_w/D_n), and ellipticity, were calculated using Atlas software (Tescan Digital Microscopy Imaging; Brno, Czech Republic) from evaluation of at least 500 individual particles from TEM micrographs by measuring long axis (morphological descriptor MaxFeret) and short axis (morphology descriptor MinFeret). The average diameters and ellipticity can be expressed as follows:

$$\text{Average diameter} = 1/2 \times (\text{MaxFeret} + \text{MinFeret}), \tag{1}$$

$$\text{Ellipticity} = \text{MaxFeret}/\text{MinFeret}, \tag{2}$$

$$D_n = \sum n_i D_i / \sum n_i, \tag{3}$$

$$D_w = \sum n_i D_i^4 / \sum n_i D_i^3, \tag{4}$$

where n_i and D_i are number and diameter of the i-th particle, respectively.

Dynamic light scattering. The hydrodynamic particle diameter (D_h), size distribution (polydispersity PI), and ζ-potential of the nanoparticles were determined using dynamic light scattering (DLS) on a ZEN 3600 Zetasizer Nano Instrument (Malvern Instruments; Malvern, UK). The particle suspension (0.1 mg ml^{-1}) was measured at 25 °C, and the data were analyzed using the Malvern software.

ATR FTIR spectroscopy. Infrared spectra were recorded on a Nexus Nicolet 870 FTIR spectrometer (Madison, WI, USA) equipped with a liquid nitrogen-cooled mercury cadmium telluride detector. The spectra were measured using a Golden Gate single reflection ATR cell (Specac; Orpington, UK) equipped with a diamond internal reflection ATR crystal.

Upconversion luminescence. Upconversion luminescence was measured on a Leica TCS SP2 AOBS confocal inverted fluorescence microscope (Mannheim, Germany) using a PL APO 100×/1.40–0.70 oil immersion objective (pinhole 1 Airy unit) and a Coherent Chameleon Ultra Ti:sapphire laser (Santa Clara, CA, USA) at 970 nm excitation. The NaGdF$_4$:Yb^{3+}/Er^{3+} nanoparticle (0.01 g) dispersions in hexane were placed on a cover glass.

Magnetic resonance. Magnetic resonance (MR) images were acquired using a 4.7 T Bruker Biospec spectrometer equipped with a commercially available resonator coil (both Bruker, Germany) at 25 °C. A standard two-dimensional rapid acquisition with a relaxation enhancement multispin echo sequence was used with the following parameters: repetition time = 280 ms, echo time = 12 ms, turbo factor = 2, spatial resolution = 137 × 137 μm^2, slice thickness = 0.7 mm, number of acquisitions = 16, and acquisition time = 9 min 36 s. The signal-to-noise ratio SNR = 0.655 S/σ, where S is signal intensity in a region of interest, σ is the standard deviation of the noise in background and constant 0.655 reflects Rician distribution of the background noise in a magnitude MR image.

The MR relaxometry was performed for different concentrations of the particles at magnetic field $B_0 = 0.5$ T and 20 °C.

3. Results and discussion

3.1 Morphology, structure, phase, and composition of NaGdF$_4$:Yb^{3+}/Er^{3+} and NaGdF$_4$:Yb^{3+}/Er^{3+}@SiO$_2$ nanoparticles

Upconversion/magnetic nanoparticles composed of NaGdF$_4$ host lattice doped with Yb^{3+} and Er^{3+} ions and stabilized with oleic acid were obtained by the high-temperature coprecipitation of lanthanide chlorides. The morphology and particle size were evaluated using the TEM microscopy (Fig. 1a). The particles exhibited an ellipsoidal shape with a mean size D_n = 27 nm and a reasonably narrow particle size distribution (PDI = 1.20). Size distribution histograms of all synthesized particles were presented in ESI (Fig. S2†). The hydrodynamic diameter of the NaGdF$_4$:Yb^{3+}/Er^{3+} nanoparticles in hexane was D_h = 35 nm with polydispersity PI = 0.28, which confirmed the relatively narrow size distribution. The difference between D_n and D_h of the NaGdF$_4$:Yb^{3+}/Er^{3+} particles can be explained by the presence of the adsorbed steric stabilizer (oleic acid) on the nanoparticle surface, which is not visible on the TEM micrographs of the particles in the dry state due to low contrast of oleic acid compared to the lanthanide particles.

Freshly synthesized NaGdF$_4$:Yb^{3+}/Er^{3+} particles are hydrophobic in nature; hence they are dispersible only in organic

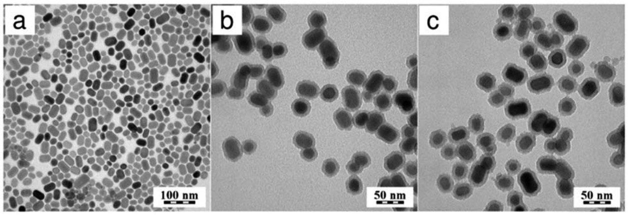

Fig. 1 TEM micrographs of (a) starting NaGdF$_4$:Yb^{3+}/Er^{3+} and (b, c) NaGdF$_4$:Yb^{3+}/Er^{3+}@SiO$_2$ nanoparticles; (b) 20 μl and (c) 40 μl TMOS in the feed.

solvents (*e.g.*, hexane), but not in water, which is required for all biological experiments. To render the particles dispersible in aqueous media, their surface was modified with a silica shell using the reverse microemulsion technique.[28] It is worth mentioning that the nanoparticle surface must be completely covered by a homogeneous silica shell without the formation of any additional pure silica particles without a core. In this report, the shell thickness of $NaGdF_4$:Yb^{3+}/Er^{3+}@SiO_2 nanoparticles was controlled by varying TMOS amount added to the mixture under otherwise constant reaction conditions, including the concentrations of the nanoparticles, NH_4OH, and Igepal CO-520. When 20 μl of TMOS was added to the reaction mixture, the nanoparticles reached 36 nm in size (PDI = 1.18), *i.e.*, they were covered by a 5 nm-thick silica shell (Fig. 1b). In contrast, the addition of a greater quantity of TMOS (40 μl) increased the particle size and shell thickness to 41 and 7 nm, respectively. However, under the latter conditions, additional pure silica particles ∼10 nm in size were formed (Fig. 1c). Therefore, further experiments were performed using the optimal amount, 20 μl of the TMOS precursor to achieve complete coverage of the nanoparticle surface with a homogeneous silica shell while avoiding the production of neat silica. The DLS measurements (D_h, PI, and ζ-potential) in water confirmed successful modification of the $NaGdF_4$:Yb^{3+}/Er^{3+} particle surface with silica. The D_h of the $NaGdF_4$:Yb^{3+}/Er^{3+}@SiO_2 particles was 65 nm (PI = 0.3), and the particles exhibited a good colloidal stability due to a total negative surface charge (−30 mV) that originated from the silanol groups.[34]

The crystal structure and elemental composition of the prepared nanoparticles were verified by TEM microscopy using selected area electron diffraction (TEM/SAED) and energy-dispersive analysis of X-rays (TEM/EDX; Fig. 2). Regardless of the SiO_2 shell, the SAED diffractograms of the nanoparticles were identical; only one representative diffraction pattern of uncoated $NaGdF_4$:Yb^{3+}/Er^{3+} nanocrystals is therefore shown on Fig. 2a. A comparison of the experimental SAED with theoretically calculated X-ray diffractograms (XRD) of known crystal structures from crystallographic databases[33] showed very good agreement between the experiment and the hexagonal phase of $NaGdF_4$ (Fig. 2b). Consequently, the most intense diffraction rings could be described (Fig. 2a) and the diffraction positions and intensities in the recalculated 1D-diffractogram were analyzed (Fig. 2b). The diffraction positions of SAED and XRD showed a perfect fit, which unambiguously confirmed that the prepared nanoparticles were the hexagonal phase of $NaGdF_4$. The diffraction intensities of the SAED and XRD exhibited certain differences that could be attributed to the quite complex preferred orientation (texture) of the nanocrystals lying on the flat, electron-transparent carbon film. The strongest SAED diffraction (*hkl*) was (101), and two additional SAED diffractions, (002) and (111), were remarkably stronger than the corresponding XRD diffractions (Fig. 2b). The first pair of strong SAED diffractions, (101) and (002), defined the first zone of strongly diffracting lattice planes that was described by the zone axis $[uvw] = [0,1,0]$ and corresponded to the first preferred orientation of nanocrystals on the carbon film. The second pair of strong SAED diffractions, (101) and (111), defined the second zone of strongly diffracting lattice planes that was described by the zone axis $[uvw] = [1,0,-1]$ and corresponded to the second preferred orientation of the nanocrystals on the carbon film (calculation of zone axes from the strong diffractions was described elsewhere[35]). As a result, the strongest experimentally observed diffractions associated with the above two zone axes should obey the Weiss Zone Law (WZL): $hu + kv + lw = 0$, where (h, k, l) are the diffraction indices of the planes, and $[u, v, w]$ are the indices of the zone axis.[35] For the first zone axis $[uvw] =$

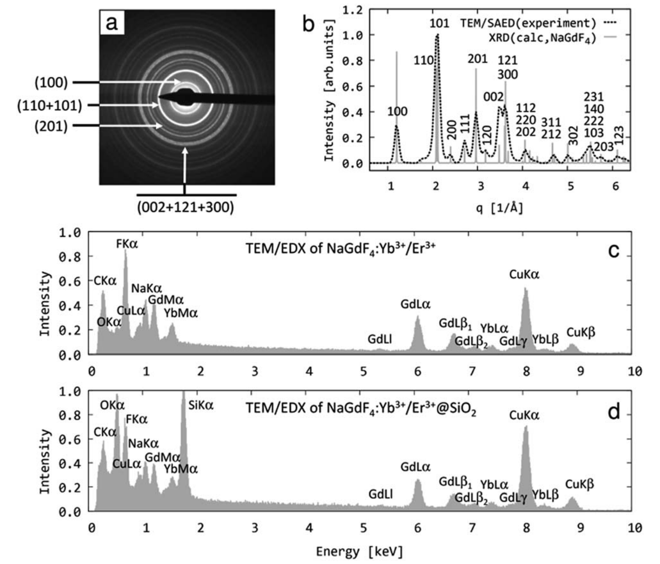

Fig. 2 (a, b) TEM analysis of the crystal structure and (c, d) the elemental composition of the prepared nanoparticles. (a) Selected area electron diffraction pattern (SAED) of $NaGdF_4$:Yb^{3+}/Er^{3+}, (b) comparison of the experimental SAED pattern with theoretically calculated X-ray diffraction pattern (XRD) corresponding to the hexagonal phase of $NaGdF_4$, and energy-dispersive spectrum (EDX) of (c) original $NaGdF_4$:Yb^{3+}/Er^{3+}, and (d) $NaGdF_4$:Yb^{3+}/Er^{3+}@SiO_2 nanoparticles.

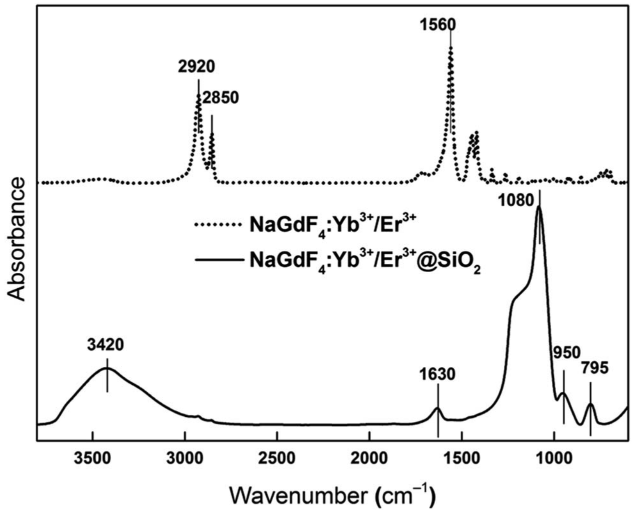

Fig. 3 ATR FTIR spectra of $NaGdF_4$:Yb^{3+}/Er^{3+} (full line) and $NaGdF_4$:Yb^{3+}/Er^{3+}@SiO_2 nanoparticles (dashed line).

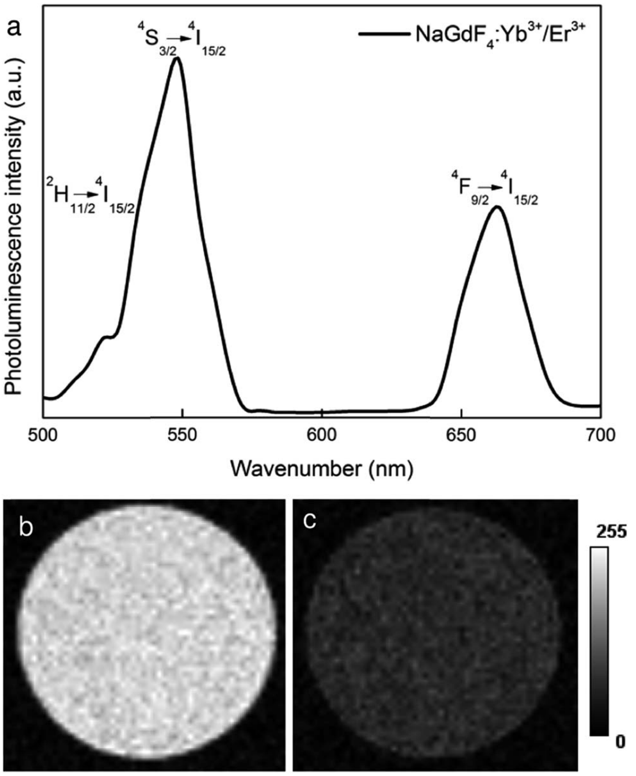

Fig. 4 (a) NIR-to-VIS emission spectrum of NaGdF$_4$:Yb^{3+}/Er^{3+} nanoparticles at 970 nm excitation. T_1-weighted MR images of (b) a phantom containing NaGdF$_4$:Yb^{3+}/Er^{3+} nanoparticles and (c) a control phantom filled with water.

[0,1,0], the WZL takes the form $k = 0$, and consequently, the strongest SAED diffractions should have indices of the type ($h0l$). For the second zone axis $[uvw] = [1,0,-1]$, the WZL takes the form $h - l = 0$, *i.e.*, $h = l$, which means that the strongest SAED diffractions should have indices of the type (hkh), *i.e.*, the first and the last diffraction indices are equal. Indeed, the four strongest SAED diffraction rings (Fig. 2a) were formed by a combination of ($h0l$) and/or (hkh) diffractions (with just one exception of strong low-angle diffraction (110)), which proved that the above analysis of preferred orientation of nanocrystals deposited on the carbon film was correct. Moreover, the stronger higher-angle diffractions were usually ($h0l$) and/or (hkh) (Fig. 2b).

Embedding of the NaGdF$_4$:Yb^{3+}/Er^{3+} nanoparticles in the SiO$_2$ shell was verified using TEM/EDX (Fig. 2c and d). The EDX spectrum of uncoated nanoparticles (Fig. 2c) showed only the peaks from the standard TEM support (carbon coated copper grid; peaks of C and Cu) and the peaks of the prepared particles (Na, Gd, and F, including the substituting Yb but lacking any of the substituting Er ions, whose concentration was below the detection limit). The very weak oxygen peak probably resulted from the slight oxidation of the carbon film. The EDX spectrum of the NaGdF$_4$:Yb^{3+}/Er^{3+}@SiO$_2$ nanoparticles exhibited the same peaks as described above plus strong peaks of the enveloping silica (Si and O; Fig. 2d).

Modification of NaGdF$_4$:Yb^{3+}/Er^{3+} nanoparticles with the silica shell was also confirmed by ATR FTIR spectroscopy (Fig. 3). The peak at 1560 cm^{-1} corresponding to the COO$^-$ band and peaks at 2850 and 2920 cm^{-1} belonging to the symmetric and asymmetric CH$_2$ stretching vibrations, respectively, confirmed the presence of oleic acid on the nanoparticle surface. After the addition of the silica shell to the NaGdF$_4$:Yb^{3+}/Er^{3+} nanoparticles, the latter bands disappeared and characteristic SiO$_2$ peaks were recorded in the spectrum of the NaGdF$_4$:Yb^{3+}/Er^{3+}@SiO$_2$ particles. The symmetric and asymmetric vibrations of Si–O–Si and Si–OH appeared at 795 and 950 cm^{-1}, respectively. The peak at 1080 cm^{-1} was attributed to the Si–O–Si stretching vibration, and the intense broad peaks at 1630 and ~3420 cm^{-1} in the spectrum of NaGdF$_4$:Yb^{3+}/Er^{3+}@SiO$_2$ were induced by the bending and stretching vibrations of the OH groups of adsorbed water molecules, respectively.

NaGdF$_4$ nanoparticles that were doped with the optically active Yb^{3+}/Er^{3+} ion pair exhibited a characteristic photoluminescence (Fig. 4a) that emitted high-energy visible photons

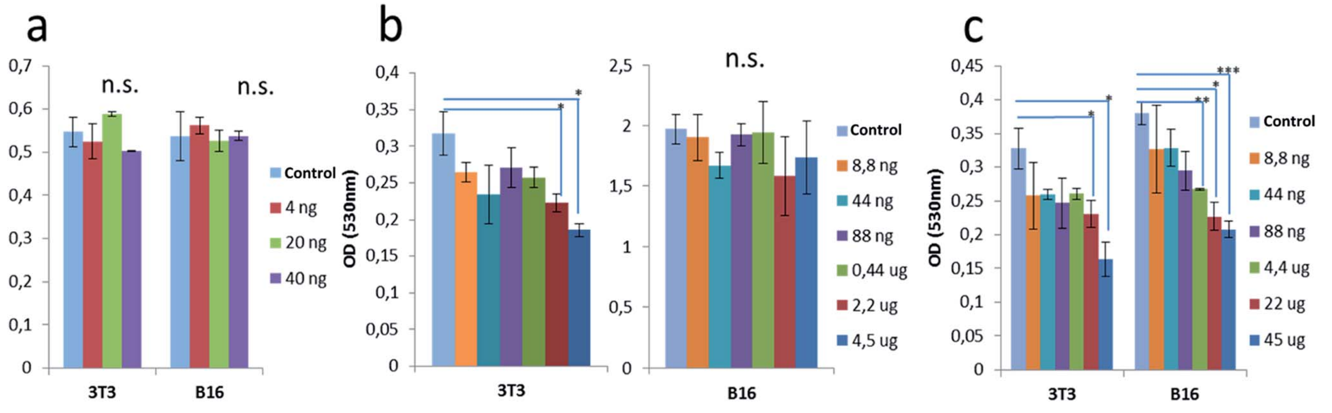

Fig. 5 The effect of increasing concentration of NaGdF$_4$:Yb^{3+}/Er^{3+}@SiO$_2$ nanoparticles (ng to µg per well containing 150 µl of cultivation medium) on the viability of non-tumor cells (3T3 mouse fibroblasts) and tumor cells (B16F10 mouse melanoma) after a 48 h incubation determined using the MTT assay. (a) 4–40 ng per well corresponding to 27–267 ng ml^{-1} and (b) 8.8 ng per well to 4.5 µg per well, corresponding to 0.06–35 µg ml^{-1}, and (c) 8.8 ng per well to 45 µg per well corresponding to 60 ng ml^{-1} to 0.35 mg ml^{-1}. OD: optical density. Student's *t*-test was considered significant for $p \geq 0.05$, *$p < 0.05$, **$p < 0.01$, and ***$p < 0.001$; n.s. = non-significant.

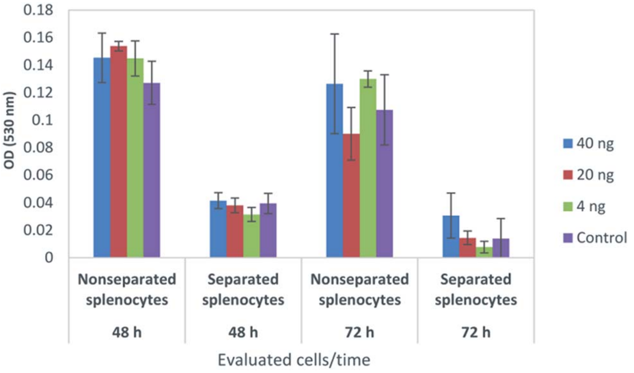

Fig. 6 Effect of increasing concentrations of NaGdF$_4$:Yb^{3+}/Er^{3+}@SiO$_2$ nanoparticles (ng per well) on the viability of immune cells obtained from the spleen homogenates of healthy mice after 48 and 72 h incubation. The viability was determined using the MTT assay. OD: optical density. No significance was found using the Student's *t*-test.

after being excited by two low-energy NIR photons *via* the energy transfer upconversion mechanism. Under NIR irradiation at 970 nm, the NaGdF$_4$:Yb^{3+}/Er^{3+} nanoparticles emitted intense green (520 and 550 nm) and red light (660 nm), which can be ascribed to $^2H_{11/2} \rightarrow {}^4I_{15/2}$, $^4S_{3/2} \rightarrow {}^4I_{15/2}$ and $^4F_{9/2} \rightarrow {}^4I_{15/2}$ radiative transitions of Er^{3+} ions, respectively, which originated from energy transfer between the Yb^{3+} and Er^{3+} ions. T_1-weighted MR images of NaGdF$_4$:Yb^{3+}/Er^{3+} particles showed a noticeable higher MR signal (3.5×) compared to that obtained from water phantoms (Fig. 4b). The SNR in the phantom containing NaGdF$_4$:Yb^{3+}/Er^{3+} nanoparticles (0.5 mg ml^{-1}) was 22.5 (the control water phantom had an SNR = 6.4). This result suggested suitable paramagnetic properties that would allow use of the NaGdF$_4$:Yb^{3+}/Er^{3+}nanoparticles as a contrast agent for magnetic resonance imaging. This was supported by the relaxometry measurements, where significant shortening of the relaxation time was observed even at low particle concentrations (Table S1†).

3.2 Viability of cells incubated with NaGdF$_4$:Yb^{3+}/Er^{3+}@SiO$_2$ nanoparticles assessed using the MTT assay

The viability of tumor and non-tumor mouse cell lines (B16F10 melanoma cells and 3T3 fibroblasts, respectively) was repeatedly investigated *in vitro* using MTT assay after 48 h of incubation with 4, 20, and 40 ng of the NaGdF$_4$:Yb^{3+}/Er^{3+}@SiO$_2$ particles per well containing 150 µl of cultivation medium (corresponding to 27, 133, and 267 ng ml^{-1}, respectively; Fig. 5a). None of these particle concentrations induced significant cytotoxicity. In further experiments, the 3T3 and B16F10 cells were incubated with progressively higher concentrations of the nanoparticles for 48 h (Fig. 5b). At concentrations ≤4.5 µg per well (corresponding to 30 µg ml^{-1}), the colloid did not cause any toxicity in the tumor cells, whereas in the range of 8.8 ng to 0.44 µg per well (corresponding to 0.06–3 µg ml^{-1}) the non-tumor cells (3T3) showed a slight reduction of viability and a progressive cytotoxic effect at 2.2 and 4.5 µg of particles per

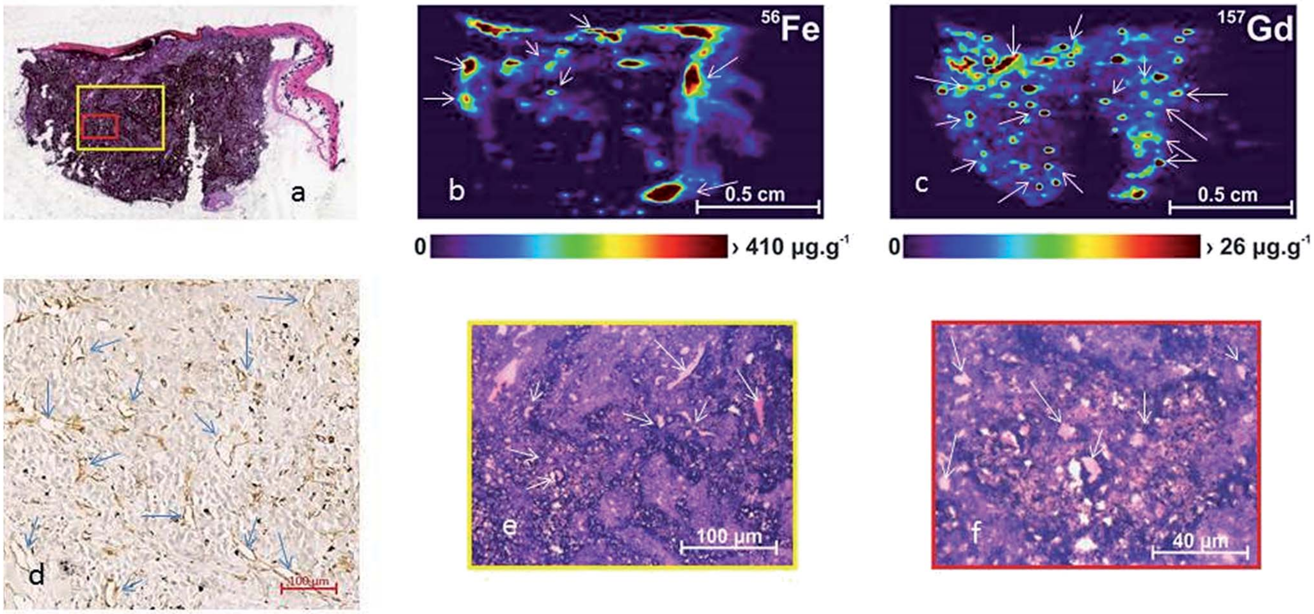

Fig. 7 The histology of melanomas in syngeneic C57BL/6 mice treated with intravenously injected NaGdF$_4$:Yb^{3+}/Er^{3+}@SiO$_2$ nanoparticles compared using LA-ICP-MS (first row). (a) Representative tumor slice stained with haematoxylin and eosin, elemental distribution map for (b) Fe, (c) Gd, (d) evidenced vascularization of melanoma tissue by endothelial staining in immunohistochemistry, (e, f) detailed histological images of LA-ICP-MS-analyzed melanoma tissue (haematoxylin–eosin staining), framed in yellow and red on the total tumor section, showing the tumor tissue with blood vessels, better evidenced by staining of vascular endothelia by immunohistochemistry methods (vessels are stained in brown). LA-ICP-MS for Fe demonstrated only the main vessels according to the Fe in the blood (hemoglobin), while the Gd analysis better revealed the details of the vascularization at an even lower concentration of the tracer than the Fe and with a very good correspondence with the vascular distribution revealed by immunohistochemistry. Arrows indicate the vessels.

well (corresponding to 15 and 30 μg ml^{-1}). The cytotoxic effect was evident and progressive with further increases in the particle concentrations in μg scale, up to 45 μg per well corresponding to 0.35 mg ml^{-1}; (Fig. 5c). In this case, both kinds of cells presented cytotoxic effect when the particle concentration was >4.4 μg per well (corresponding to 0.03 mg ml^{-1}). Interestingly, the toxic effect was more relevant on tumor cells.

Additional experiments were performed to evaluate the effects of various $NaGdF_4$:Yb^{3+}/Er^{3+}@SiO_2 nanoparticle concentrations on the viability of immune cells after 48 and 72 h of cultivation. Immune cells were obtained from the spleens of healthy C57BL/6 mice after spleen homogenization. The complete suspension consisting of lymphocytes and myeloid cells was compared with a purified lymphocyte suspension obtained by density gradient separation with Ficoll-Paque™. This was performed because lymphocytes co-cultivated with myeloid cells are more resistant than those after separation. Therefore, the separated lymphocyte suspension was expected to be more sensitive to possible cytotoxic agents. The incubation with $NaGdF_4$:Yb^{3+}/Er^{3+}@SiO_2 nanoparticles at concentrations 4–40 ng per well (27–267 ng ml^{-1}) did not produce a significant change in the cell viability in either preparations even after 72 h of culture. As expected, the viability of the isolated lymphocytes was lower than that of the non-separated cells, but in neither case did the doses of $NaGdF_4$:Yb^{3+}/Er^{3+}@SiO_2 nanoparticles induce cytotoxicity (Fig. 6).

3.3 Localization of $NaGdF_4$:Yb^{3+}/Er^{3+}@SiO_2 nanoparticles in mouse organs

The distribution of the $NaGdF_4$:Yb^{3+}/Er^{3+}@SiO_2 nanoparticles in the tumor and body tissues was evaluated using LA-ICP-MS, which is a powerful analytical technique for highly sensitive direct examination of the content of elements, in the present case Gd, in biological tissues. The Fe present in the hemoglobin was evaluated for comparison. The experiments were performed in the tumor tissue (melanoma) and healthy tissue (brain and liver) in a mouse model after intravenous administration of

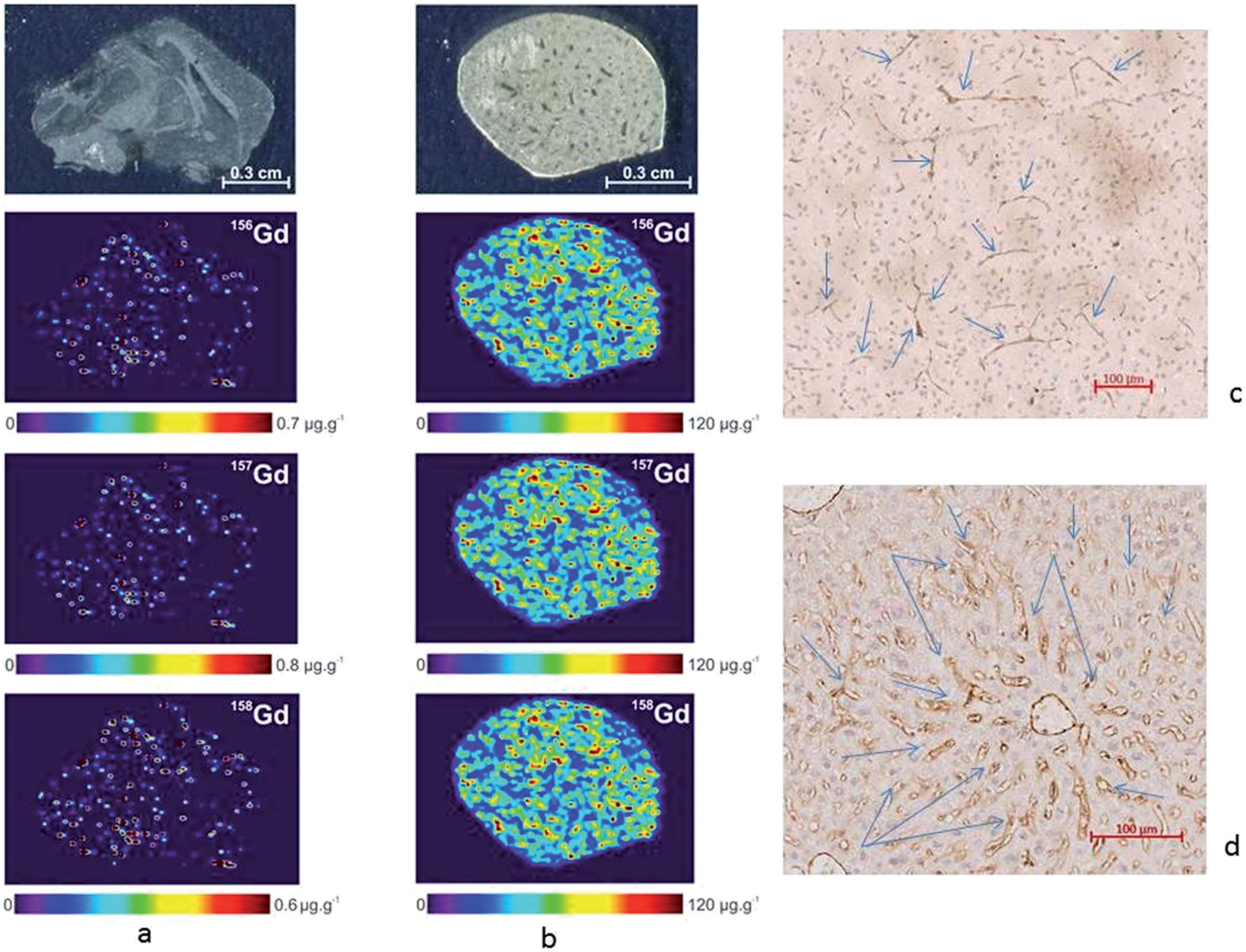

Fig. 8 Elemental distributions of gadolinium isotopes (^{156}Gd, ^{157}Gd, ^{158}Gd) in the brain (left) and liver vessels (right) after treatment of the tumor-bearing mice with $NaGdF_4$:Yb^{3+}/Er^{3+}@SiO_2 nanoparticles. LA-ICP-MS imaging data were collected with a 110 μm laser focus. The optical images of the analyzed tissue sections (top, grey) were obtained using a Scanner HP Scanjet 4890 with the resolution of 4800 dpi. LA-ICP-MS imaging shows accumulation of the particles at the vascular level according to the vascular distribution in the tissues, as confirmed by the immunohistochemistry (vessels stained in brown are indicated by arrows).

a standard concentration of the $NaGdF_4:Yb^{3+}/Er^{3+}@SiO_2$ nanoparticles. First, the tumor localization was evaluated. The $NaGdF_4:Yb^{3+}/Er^{3+}@SiO_2$ nanoparticles (100 μl of a colloid; 2 mg of particles per ml diluted 1 : 50 in PBS) were injected into animals harboring murine B16F10 melanoma cells. As described in the Experimental section, sequential sections of frozen samples were prepared and analyzed to permit comparison of the histological picture (Fig. 7a, d and e) with the LA-ICP-MS analysis. The LA-ICP-MS images showed that the Fe was predominantly associated with large blood vessels due to high amounts of Fe present in hemoglobin (Fig. 7b) and a high background. In contrast, the Gd accumulation better defined the vascular component of the tumor tissue. The Gd signal was apparent at a much lower particle concentration (26 μg g^{-1}) than the Fe signal (410 μg g^{-1}; Fig. 7b and c). Many blood vessels with accumulated $NaGdF_4:Yb^{3+}/Er^{3+}@SiO_2$ particles can be seen in Fig. 7d. These nanoparticles have thus the substantial advantages of having a very low background and highly sensitive demonstration of blood vasculature as long as 48 h after the injection.

Second, the brain and liver tissues were analyzed, and the $NaGdF_4:Yb^{3+}/Er^{3+}@SiO_2$ particles were distinctly detected in the vasculature net (Fig. 8). In the brain, the $NaGdF_4:Yb^{3+}/Er^{3+}@SiO_2$ particles were present only in the blood vessels (Fig. 8a). In contrast, very high accumulation of the $NaGdF_4:Yb^{3+}/Er^{3+}@SiO_2$ nanoparticles was observed in the vascular and perivascular spaces of the liver, as indicated by the presence of some background (Fig. 8b). This was expected because it is known that the Kupffer cells can easily take up circulating particles.[36] Chronic accumulation of the particles may represent a problem, especially within the kidneys, on the basis that Gd contrast agents, which are widely used in MRI studies, have been often associated with a risk of systemic toxicity and fibrosis in patients with reduced renal function.[37] However, the nanoparticle formulation may take advantage of the liver detoxification ability, implying that the particles are eventually removed and engulfed by macrophages.

4. Conclusions

Rare-earth upconversion nanocrystals with a thin silica coating layer, $NaGdF_4:Yb^{3+}/Er^{3+}@SiO_2$ particles, have been successfully prepared. Their morphology, composition, structure, and coating were verified by detailed TEM analysis, including energy dispersive spectroscopy (EDX) and electron diffraction (SAED). The comparison of experimental SAED diffraction patterns with theoretically calculated XRD patterns proved unambiguously that the prepared nanocrystals had a crystalline structure of hexagonal $NaGdF_4$. The upconversion property in combination with an immobilized photosensitizer, namely, the emission of red/green light after irradiation with deep-tissue penetrating NIR light, is very important for future applications of the particles in photodynamic tumor therapy. Moreover, Gd renders the particles, when accumulated by efficient EPR effect, with contrast in MRI, which may permit non-invasive detection of $NaGdF_4:Yb^{3+}/Er^{3+}@SiO_2$ particle-engulfed cells of pathological sites in the organism.

Biological experiments confirmed that the cytotoxicity of $NaGdF_4:Yb^{3+}/Er^{3+}@SiO_2$ nanoparticles was dose-related with a threshold above 0.5 μg of particles per well (3 μg ml^{-1}) and clearly present at concentrations of 2.2 μg per well (15 μg ml^{-1}). Lower concentrations did not affect the viability of non-tumor, tumor, or immune cells. The LA-ICP-MS method proved to be very effective for the direct determination of the $NaGdF_4:Yb^{3+}/Er^{3+}@SiO_2$ particle distribution within the biological tissues. This technique enables visualization of even very small quantities of the particles (pico- to femtograms), thus facilitating highly sensitive (parts per billion) monitoring of the nanoparticle distribution inside a tissue. In this manner, the distribution of blood vessels containing $NaGdF_4:Yb^{3+}/Er^{3+}@SiO_2$ nanoparticles within the tumor was easily visualized. Even a very small quantity of accumulated particles was detectable, which is beneficial in terms of injection of very low particle doses. This might be applicable even in biopsies of investigated organs or tumor tissues, allowing extensive evaluation of the nanoparticle distribution in the organism to improve planning of highly precise theranostic interventions. A huge difference in the nanoparticle accumulation was found between brain and liver according to their vascular characteristics. The LA-ICP-MSI method may also be suitable for studies of the bio-distribution of the nanoparticles. In fact, the nanoparticles are actively investigated not only for therapeutic purposes[38] but also in terms of undesirable particle penetration into the organs, such as the lung and brain, due to the environmental pollution, as well as particle accumulation/elimination by the reticulo-endothelial system.[39,40]

Our investigation provides the first useful information on the biocompatibility of the newly synthetized $NaGdF_4:Yb^{3+}/Er^{3+}@SiO_2$ nanoparticles and their vascular localization in the evaluated organs even 24 h after the administration. This is important for prospective applications of Gd compounds not only for MRI, but also for efficient targeting of pathological neoangiogenesis (cancer, diabetic retinopathy, *etc.*) and micro-environmental components of cancers. Moreover, $NaGdF_4:Yb^{3+}/Er^{3+}@SiO_2$ particles can be proposed for bi-modal upconversion luminescence/MR imaging and photodynamic therapy[41] and, after functionalization or coupling with other molecules, as radiosensitizers for enhanced radiotherapy,[42] or neutron capture therapy,[43] as well as therapeutic carriers.

Conflicts of interest

There are no conflicts to declare.

Ethical statement

All procedures were conducted in strict accordance with the European Convention for the Care and Use of Laboratory Animals, and were approved by the Animal Care and Use Committee at the Institute of Microbiology, AS CR, approval ID: 64/2015.

Acknowledgements

The financial support of the Czech Science Foundation (15-01897S) is gratefully acknowledged. The biological experiments were supported by RVO 61388971 Institutional Grant and MŠMT COST CZ LD 15135, in the frame of TD1301 MiMed COST Action. Support for the electron microscopy experiments by the Technology Agency of the Czech Republic (TE01020118) is also acknowledged. The MR experiment was supported by the Ministry of Health of the Czech Republic (Institute for Clinical and Experimental Medicine, project IN 00023001).

References

1 B. Zhou, B. Shi, D. Jin and X. Liu, *Nat. Nanotechnol.*, 2015, **10**, 924.
2 Y. Zhang, W. Wei, G. K. Das and T. T. Y. Tan, *J. Photochem. Photobiol., C*, 2014, **20**, 71.
3 B. R. Smith and S. S. Gambhir, *Chem. Rev.*, 2017, **117**, 901.
4 R. Naccache, P. Chevallier, J. Lagueux, Y. Gossuin, S. Laurent, L. Vander Elst, C. Chilian, J. A. Capobianco and M. A. Fortin, *Adv. Healthcare Mater.*, 2013, **2**, 1478.
5 L. Zhou, X. Zheng, Z. Gu, W. Yin, X. Zhang, L. Ruan, Y. Yang, Z. Hu and Y. Zhao, *Biomaterials*, 2014, **35**, 7666.
6 J. Key and J. F. Leary, *Int. J. Nanomed.*, 2014, **9**, 711.
7 Y. I. Park, J. H. Kim, K. T. Lee, K. S. Jeon, H. B. Na, J. H. Yu, H. M. Kim, N. Lee, S. H. Choi, S. I. Baik, H. Kim, S. P. Park, B. J. Park, Y. W. Kim, S. H. Lee, S. Y. Yoon, I. C. Song, W. K. Moon, Y. D. Suh and T. Hyeon, *Adv. Mater.*, 2009, **21**, 4467.
8 C. Liu, Y. Hou and M. Gao, *Adv. Mater.*, 2014, **26**, 6922.
9 F. Zhang, *Photon Upconversion Nanomaterials*, Springer, 2015.
10 F. Wang, Y. Han, C. S. Lim, Y. H. Lu, J. Wang, J. Xu, H. Y. Chen, C. Zhang, M. H. Hong and X. G. Liu, *Nature*, 2010, **463**, 1061.
11 A. Sedlmeiera and H. H. Gorris, *Chem. Soc. Rev.*, 2015, **44**, 1526.
12 J. C. Boyer, M. P. Manseau, J. I. Murray and F. van Veggel, *Langmuir*, 2010, **26**, 1157.
13 H. Hu, M. X. Yu, F. Y. Li, Z. G. Chen, X. Gao, L. Q. Xiong and C. H. Huang, *Chem. Mater.*, 2008, **20**, 7003.
14 H. S. Qian, H. C. Guo, P. C. L. Ho, R. Mahendran and Y. Zhang, *Small*, 2009, **5**, 2285.
15 R. Naccache, F. Vetrone, V. Mahalingam, L. A. Cuccia and J. A. Capobianco, *Chem. Mater.*, 2009, **21**, 717.
16 L. W. Yang, Y. Y. Zhang, J. J. Li, Y. Li, J. X. Zhong and P. K. Chu, *Nanoscale*, 2010, **2**, 2805.
17 T. A. Rose Jr and J. W. Choi, *Am. J. Med.*, 2015, **128**, 943.
18 A. K. Alshememry, S. S. El-Tokhy and L. D. Unsworth, *Curr. Pharm. Des.*, 2017, **23**, DOI: 10.2174/1381612823666170522100545.
19 C. Xu, Y. Wang, C. Zhang, Y. Jia, Y. Luo and X. Gao, *Nanoscale*, 2017, **9**, 4620.
20 A. C. Anselmo and S. Mitragotri, *AAPS J.*, 2015, **17**, 1041.
21 L. Vannucci, E. Falvo, M. Fornara, P. Di Micco, O. Benada, J. Krizan, J. Svoboda, K. Hulikova-Capkova, V. Morea, A. Boffi and P. Ceci, *Int. J. Nanomed.*, 2012, **7**, 1489.
22 L. Vannucci, E. Falvo, C. M. Failla, M. Carbo, M. Fornara, R. Canese, S. Cecchetti, L. Rajsiglova, D. Stakheev, J. Krizan, A. Boffi, G. Carpinelli, V. Morea and P. Ceci, *J. Biomed. Nanotechnol.*, 2015, **11**, 81.
23 J. Elgqvist, *Int. J. Mol. Sci.*, 2017, **18**, 1102.
24 H. Hashizume, P. Baluk, S. Morikawa, J. W. McLean, G. Thurston, S. Roberge, R. K. Jain and D. M. McDonald, *Am. J. Pathol.*, 2000, **156**, 1363.
25 J. A. Barreto, W. O'Malley, M. Kubeil, B. Graham, H. Stephan and L. Spiccia, *Adv. Mater.*, 2011, **23**, H18.
26 H. H. Shen, E. C. Chan, J. H. Lee, Y. S. Bee, T. W. Lin, G. J. Dusting and G. S. Liu, *Nanomedicine*, 2015, **10**, 2093.
27 U. Kostiv, O. Janoušková, M. Šlouf, N. Kotov, H. Engstová, K. Smolková, P. Ježek and D. Horák, *Nanoscale*, 2015, **7**, 18096.
28 U. Kostiv, I. Kotelnikov, V. Proks, M. Šlouf, J. Kučka, H. Engstová, P. Ježek and D. Horák, *ACS Appl. Mater. Interfaces*, 2016, **8**, 20422.
29 U. Kostiv, V. Patsula, M. Šlouf, I. Pongrac, S. Škokić, M. Dobrivojević Radmilović, I. Pavičić, I. Vinković Vrček, S. Gajović and D. Horák, *RSC Adv.*, 2017, **7**, 8786.
30 L. Miao and L. Huang, *Cancer Treat. Res.*, 2015, **166**, 193.
31 J. L. Lábár, *Ultramicroscopy*, 2005, **103**, 237.
32 W. Kraus and G. Nolze, *J. Appl. Crystallogr.*, 1996, **29**, 301.
33 L. Glasser, *J. Chem. Educ.*, 2016, **93**, 542.
34 D. Fairhurst and R. W. Lee, *Drug Dev. Delivery*, 2011, **11**, 60.
35 K. W. Andrews, D. J. Dyson and S. R. Keown, *Interpretation of Electron Diffraction Patterns*, Plenum Press, 1967.
36 E. Sadauskas, H. Wallin, M. Stoltenberg, U. Vogel, P. Doering, A. Larsen and G. Danscher, *Part. Fibre Toxicol.*, 2007, **4**, 10.
37 D. J. Todd and J. Kay, *Annu. Rev. Med.*, 2016, **67**, 273.
38 P. Muralidharan, M. Malapit, E. Mallory, D. Hayes Jr and H. M. Mansour, *Nanomedicine*, 2015, **11**, 1189.
39 J. Morton, E. Tan and S. K. Suvarna, *J. Trace Elem. Med. Biol.*, 2016, **43**, 63.
40 E. Principi, R. Girardello, A. Bruno, I. Manni, E. Gini, A. Pagani, A. Grimaldi, F. Ivaldi, T. Congiu, D. De Stefano, G. Piaggio, M. de Eguileor, D. M. Noonan and A. Albini, *Int. J. Nanomed.*, 2016, **11**, 4299.
41 J. Liu, L. Huang, X. Tian, X. Chen, Y. Shao, F. Xie, D. Chen and L. Li, *Int. J. Nanomed.*, 2016, **12**, 1.
42 S. Kotb, A. Detappe, F. Lux, F. Appaix, E. L. Barbier, V. L. Tran, M. Plissonneau, H. Gehan, F. Lefranc, C. Rodriguez-Lafrasse, C. Verry, R. Berbeco, O. Tillement and L. Sancey, *Theranostics*, 2016, **6**, 418.
43 N. Protti, S. Geninatti-Crich, D. Alberti, S. Lanzardo, A. Deagostino, A. Toppino, S. Aime, F. Ballarini, S. Bortolussi, P. Bruschi, I. Postuma, S. Altieri and H. Nikjoo, *Radiat. Prot. Dosim.*, 2015, **166**, 369.